Tuning optical/electrical properties of 2D/3D perovskite by the inclusion of aromatic cation

Jesús Rodríguez-Romero,[a] Bruno Clasen Hames,[a] Pavel Galar,[b] Azhar Fakharuddin,[c] Isaac Suarez,[d] Lukas Schmidt-Mende,[c] Juan P. Martínez-Pastor,[d] Abderrazzak Douhal,[b] Iván Mora-Seró,[a]* and Eva M. Barea.[a]*

a Institute of Advanced Materials (INAM), Universitat Jaume I, 12006 Castelló, Spain

b Departamento de Química Física, Facultad de Ciencias Ambientales y Bioquímica, and INAMOL, Universidad de Castilla-La Mancha, Avenida Carlos III, S.N., 45071 Toledo, Spain

c Department of Physics. University of Konstanz. 78457 Konstanz, Germany

d UMDO, Instituto de Ciencia de los Materiales, Universidad de Valencia, Valencia 46071, Spain.

Email: sero@uji.es, barea@uji.es

Abstract

The application of bulky aliphatic cations in the manufacture of moisture´s stable materials has triggered the development and application of 2D/3D perovskites as sensitizers in stable to moisture solar cells. While it is true the moisture´s stability increases, it is also true that the photovoltaic performance of the 2D/3D PVK material is severely limited owing to quantum and dielectric confinement effects. Accordingly, it is necessary the synthesis and deep optical characterization of materials with an adequate management of dielectric contrast between the layers. Here, we demonstrate the successful dielectric confinement tuning by the inclusion of a conjugated molecule, as bulky cation, in the fabrication of 2D/3D PVK material $(C_6H_5NH_3)_2(CH_3NH_3)_{n-1}Pb_nI_{3n+1}$ where n=3 and 5. The absence of excitonic states related to n≥1 at room temperature, as well as the very low concentration of excitons after 1 ps for samples where n≥3, are a strong evidence of an excellent ability to dissociate excitons in free charge carriers. As consequence films with low n presenting higher stability than standard 3D perovskites, improve significantly their performance showing one of the highest short circuit current density (J_{sc}≈13.8) obtained to date for perovskite materials within the 2D limit (n<10).
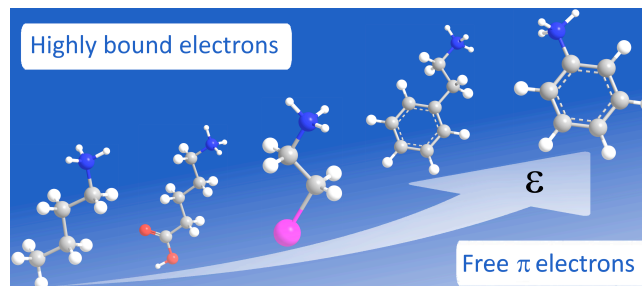
Introduction

During the last years, hybrid organic-inorganic halide perovskites (PVK), ABX_3 where A=methylammonium, formamidinium; B=Pb, Sn, Ge; X=Br, I are continuously making breakthroughs in optoelectronic devices spanning photovoltaics, light emitting, lasers and photodetectors owing to their unique optical and electrical properties. (1, 2) Their performance in perovskite solar cells (PSCs) has been exceptionally remarkable, solution processed devices now deliver power conversion efficiency (PCE) close to 23%.(3) However, challenges such as stability under environmental conditions need to be addressed thinking in commercial application.(4, 5)

The inclusion of bulky hydrophobic organic cations, in perovskite´s chemical formulation, is one of the most successful strategies followed to overcome the issue related to stability towards moisture. The generated material adopts a layered arrangement named 2D or 2D/3D PVK of general chemical formula $R_2R´_{n-1}Pb_nX_{3n+1}$ (R=aryl-, alkyl- cation, R´=methylammonium, formamidinium, etc; X=Cl, Br I and n=number of inorganic layers). This structural arrangement adopts the form of a natural multi quantum well structure, producing two important phenomena: 1) the excitons (or charge carriers) are confined to inorganic layers (the wells) owing to a very different band gap compared to the organic layers (the barriers); consequently, it is possible to see highly stable excitonic transition, with high binding energy, inclusive at room temperature (quantum confinement effect); and 2) a stronger difference in dielectric properties between the inorganic and organic layers produce a still more intense coulombic interaction of the exciton than systems where a less pronounced dielectric contrast is observed (dielectric effect). (6) The dielectric mismatch, and its effects in the exciton binding energy, has been described previously by Ishihara.(7, 8) From that study, it is possible determine that the dielectric confinement can be modulated through the organic cation. Several works have been reported where bulky cations have been successfully applied in the synthesis of layered materials, with applications in solar cells highly moisture´s stable.(9-11) Despite that stability of the device is improved, the poor photovoltaic performance of the 2D/3D PVK material confirms the disadvantages related to quantum and dielectric confinements effects. A quick glance at the reported results, it becomes evident that the principal reason should be related to the aliphatic nature of all the cations used. The Fig. S1 shows the chemical structure of the principal bulky cations used in the fabrication of solar cells. These organic molecules are

represented by butylammonium (BA) (and propyl, not showed) iodide, (11-14) valeric acid derived ammonium iodide (AVA), (15) 2-iodoethylammonium iodide (EA),(16) phenylethylammonium bromide (17) or iodide (9, 18) and anilinium iodide.(19) Recently, it was demonstrated that the inclusion of polarizable guests, within crystal lattice of 2D materials, leads to a significant reduction of the excitons´ confinement, owing to a very important decrease in the exciton binding energy.(20) Analyzing the polarizability as key parameter to improve the photovoltaic performance through decreasing the exciton binding energy, the aliphatic derivatives (BA or propyl, the later not showed), have just σ-electrons located between the non-polar covalent bonds (C-C), such that the polarizability (ε) is very low. Conversely, the inclusion of aromatic rings, with free and polarizable π electrons, lead to a higher ε than the observed in aliphatic chains.(7, 19) The case of AVA(15) and EA(16) is very interesting. In spite of their structures are formed by a non-polar carbon backbone, with slightly polarizable electrons clouds (butyl and ethyl chains), the inclusion of the acid (COOH) and iodide functionalities confer them a polarizable fragment.

In a previous work, we demonstrated that photovoltaic devices, based on anilinium (Any) 2D and 2D/3D perovskite,(19) exhibit a higher performance than the ones prepared with BA cation, especially due to the higher photocurrent exhibited by the former. Based on that result and considering that the choice of the bulky cations has direct implications not only in the improved stability but also in the global both electronic and photovoltaic performance of devices, we focused our efforts in a complete optical and morphological characterization of a new type of material, with the principal hypothesis of reduce the stronger effects, as high exciton binding energy, through the modulation of dielectric contrast by the introduction of a bulky cation with free and polarizable π-electrons. Steady state and transient absorption measurements were used to study energy structure and dynamics of photoexcited charge carriers to verify the differences in internal charge carrier processes between our samples and traditional 2D/3D PVK. We have showed that our samples are capable of efficient dissociation of initially generated excitons that is in agreement with expectation of low exciton binding energy. Posteriorly, we focused our efforts on the fabrication of a 2nd generation of $Any_2MA_4Pb_5I_{16}$ 2D/3D perovskite based solar cells through hot-casting method. It was demonstrated the positive´s effect of the temperature in the materials properties with a direct correlation between temperature with the crystal sizes and PCE.

Our champion device, fabricated at T=190 °C, shows a PCE of 7.63% with a J_{sc}=13.79 mAcm^{-2}. Additionally, stability studies show that 2D/3D anilinium perovskite-based films exhibit a moderately higher resistance to environmental conditions compared to 3D perovskites based solar cells.

Experimental Section

Materials. PbI$_2$ (99.999%) was purchased to TCI. Anilinium iodide and TiO$_2$ paste (30 NR-D) and MAI were purchased to Greatcell solar company. Diisopropoxide bis(acac) solution (75% in 2-propanol), 4-tert-butylpyridine, bis-(trifluoromethylsulfonyl)imide, ethanol, acetonitrile, chlorobenzene, dimethylsulfoxide (DMSO) and dimethylformamide (DMF) were purchased to Sigma-Aldrich. All reagents were used without further purification.

Film/device characterization. The XRD pattern of the prepared films were measured using X-ray diffractometer (D8 Advance, Bruker-AXS) (Cu Kα, wavelength λ=1.5406 Å) within the range of 3-40°, step of 0.04° and counting time of 3 seconds per step. Scanning electron microscopy (SEM) images were obtained using a Jeol, JEM-3100F field emission gun scanning electron microscope with an energy range of 15 kV. Surface coating percentage was based on shaded threshold method using imageJ software. Absorbance spectra were evaluated with a UV/VIS Varian 20 Cary 300 BIO spectrophotometer. Photovoltaic devices were characterized using a Sun 2000 system solar simulator from Abet technologies. The light intensity was adjusted to 100 mWcm^{-2} using a calibrated Si solar cell. Anilinium cells prepared at 130 ºC and 150 ºC and 3D perovskite as a reference cell were characterize by Impedance Spectroscopy (IS). The measurements were carried out under an irradiation of 1 sun (AM 1.5 conditions), and different bias potentials that ranged from zero to open circuit voltage and frequencies between 1 MHz and 0.1Hz with an AC signal of 20 mV. Devices were measured using two masks to define an active area of 0.101 and 0.12 cm^2 represented values have been properly normalized to area.

Film fabrication for optical characterization (TAS). The films were prepared on glass previously treated in the UVO antechamber (15 min). After that, the glasses were heated at 130 °C during 30 min and moved directly to the spin coater for perovskite deposition after heating, with no cooling down period just the transport from the hot plate to the spin coater. The corresponding solutions of Any$_2$MA$_{n-1}$Pb$_n$I$_{3n+1}$, with n=3, 5

were warmed at 70 °C. The perovskite layers were deposited through spin coating process of 0.225 M precursor solution (50 µL) at 5000 rpm: 5000 acceleration: 20 s. Then they were annealed at 100 °C during 10 min. Perovskite precursor solutions were prepared by addition of the necessary amount of the respective reagents to obtain a 0.225 M solution with respect to PbI_2 in 1 mL of DMF and 0.095 mL of DMSO. Promptly, a layer of PMMA, (1.8 mg/1 mL chlorobenzene) was deposited at 2000 rpm/2000 acceleration, 45 s.

Femtosecond Transient Absorption Measurements. The setup used for femtosecond TA experiments was composed mainly of a regenerative amplifier (Legend-USP, Coherent) and optical parametric amplifier (OPA, CDP System). This laser system generates the pumping (70 fs, 1 – 7 mW, 400, 500, 600 and 700 nm, 1 kHz) and probing (50 fs, 1W, 800 nm, 1kHz) laser beams that was used to generate probing white light. The pump fluence of the absorbed photons ranged from 8.2×10^{12} to 9.0×10^{12} ph/cm^2 (intensity ~ 90 – 100 µW). All the presented spectra are chirp corrected. The measured instrument response function (IRF) of the system was ~ 70 fs. All the experiments were performed at 293 K.

Photoluminescence (PL) and Time Resolved PL (TRPL) as a function of temperature. Borosilicate glass was exposed to $UV-O_3$ during 10 min. A compact layer of TiO_2 was deposited on the substrates by spray pyrolysis process of titanium diisopropoxide bis(acac) solution (75% in 2-propanol, Sigma-Aldrich) diluted with absolute ethanol in 1:9 v/v proportion, respectively. The 2D/3D perovskite films were deposited in similar way that the described in the past paragraph. Posteriorly, samples were placed in the cold finger of a commercial closed cycle cryostat (ARS DE-202) that allows a temperature variation in the range 20 - 300 K. The excitation laser for time-integrated PL and TRPL measurements was a 200 fs pulsed Ti:sapphire (Coherent Mira 900D, 76 MHz of repetition rate) tuned at 808 nm and doubled to 404 nm with a BBO crystal. The backscattered PL signal was dispersed by a double 0.3-m focal length grating spectrograph/spectrometer and detected by an Andor Newton 970 EMCCD camera (for time-integrated PL spectra) placed at the exit of the second spectrometer and by a Si Micro Photon Device (MPD) single photon avalanche diode (SPAD) photodetector connected at the exit of the first monochromator; this SPAD was attached to a time correlated single photon counting electronic board (TCC900 from Edinburgh Instruments) for TRPL measurements.

Morphology and conductivity investigation using Atomic Force Microscopy. The morphology of the films was investigated using AFM (Concept Scientific Instrument) in resonant mode. The surface potential of the perovskite films were measured using KPFM mode, with an applied electrostatic bias 1V in single pass mode. The current maps of the films were recorded in cAFM mode using a diamond coated tip at an applied bias of 4V in N_2 flow. In absence of N_2, the results are often not reproducible.

Device fabrication method. Fluorine doped tin oxide (FTO) substrates were partially treated with Zn and HCl 2M and further cleaned with soap (Hellmanex) and deionized water, followed by sonication in a) ethanol and b) *i*-PrOH during 15 min for each step, and dried with compressed air. Then, the resultant substrates were exposed to UV-O_3 during 10 min. A compact layer of TiO_2 was deposited on the substrates by spray pyrolysis process of titanium diisopropoxide bis(acac) solution (75% in 2-propanol, Sigma-Aldrich) diluted with absolute ethanol in 1:9 v/v proportion, respectively. The mesoporous TiO_2 layer was deposited through spin-coating method of a suspension prepared from DYESOL-30NRD paste, diluted with absolute ethanol. After drying at 100 °C during 10 min the substrates were gradually heated to 500 °C and cooled to room temperature. The perovskite absorber layers were deposited through spin coating process of 0.225 M precursor solution at 5000 rpm for 20 s. The perovskite precursor solutions were prepared by addition of 0.1136 g of PbI_2, 0.0218 g of anilinium iodide and 0.0313 g of methylammonium iodide (MAI) in a mixture of 1 mL of DMF and 0.095 mL of DMSO. We use a modified methodology of the successful hot casting process. The perovskite precursor solution was heated to 70 °C during all the process. On the other hand, the substrates with a compact/mesoporous layer of TiO_2 were heated at 110 °C, 130 °C, 150 °C, 170 °C and 190 °C during 10 min before to start the deposition of the respective perovskite layer. Once the perovskite was deposited by spin-coating process (50 μL; 5000 rpm without acceleration; 20 s), the respective substrates were heated 10 min more at 100 °C. The substrates should show layer´s coloration since green-brown to dark brown, depending on its fabrication´s temperature. After the substrates were cooled down to room temperature the hole transporting layer (HTL) was deposited by spin coating at 4000 rpm during 30 s. The HTM was prepared dissolving 72.3 mg of (2,2′,7,7′-tetrakis(N,N-di-p-methoxyphenylamine)-9,9-spirobifluorene)(spiro-OMeTAD), 28.8 μL of 4-tert-butylpyridine, and 17.5 μL of a stock solution of 520 mg/mL lithium bis-(trifluoromethylsulfonyl)imide in acetonitrile

in 1 mL of chlorobenzene. Finally, 60 nm of gold was thermally evaporated in the vacuum chamber on top of the device to form the electrode contacts. The complete device fabrication was carried outside the globe box.

Results and discussion

As first step, we focused on the fabrication of thin films with formula $Any_2MA_{n-1}Pb_nI_{3n+1}$, hereafter $AnyPb_n$, with n=3 and 5 and their morphological characterization by X-ray diffraction XRD and scanning electron microscopy SEM. Although the n=1 film represents exactly the 2D material his low absorption across the visible range restricts his application as sensitizer in useful photovoltaic devices. XRD pattern and SEM images of thin films prepared by hot-casting method(11) are shown in the Fig. 1, (for methods see SI). The XRD patterns for both materials display peaks at 14.2 and 28.5°. These peaks have been associated to horizontal (111) and vertical (202) preferential growth in 2D perovskites.(12, 21) Additional peaks located at 20.1 and 31.9° rises with n, and they have been associated to (112) and (312) planes, respectively, in 3D perovskite.(22) Morphological characterization by SEM, demonstrate that the nucleation points are composed by leaf type grains with an impressive size over 1 μm. It is evident that the particle´s size rises with n, together with the percentage surface coating. The determined values are approximately 47 and 67%, for n=3 and 5, respectively (Fig. S2).

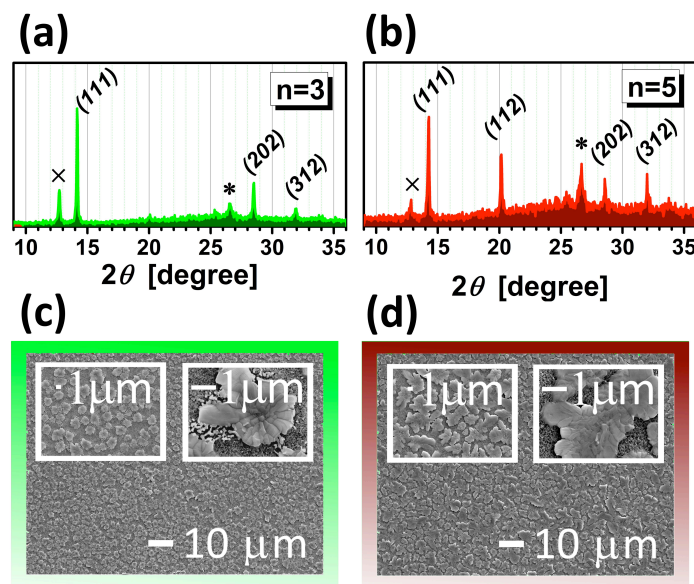**Fig. 1** Morphological characterization by XRD and SEM. (a y c) $Any_2MA_2Pb_3I_{10}$, (b y d) $Any_2MA_4Pb_5I_{16}$. *FTO ^{x}PbI$_2$

Regard the optical properties, the absorbance spectra of 2D PVK films (n=1-5) chemically formed just by aliphatic chains,(12, 14) and inclusive phenylethylammonium,(9, 18) (see Fig. S1) are characterized by an easily recognized exciton transition at the edge of the absorption band, exhibiting a red-shift progression on going from lower to higher n.(9, 12, 18, 23) Such intense excitonic absorption, with huge oscillator strength, was related to an intense Coulomb interaction between the charge carriers and, therefore, a very large exciton binding energy, affecting negatively the photovoltaic performance.(24) Unlike previous reports, the absorbance spectra of our material exhibits a direct red shift to 760 nm for both n=3 and 5, without observing traces of QW-like optical transitions. On the other hand, the photoluminescence (PL) spectra, measured for n=3 and 5 at room temperature, are practically identical (Fig. 2a, b). The main PL peak detected at ≈ 770 nm is close to reported values for 3D PVK. In addition, both films exhibit a very similar PL temperature-dependent behavior (Fig. S3).
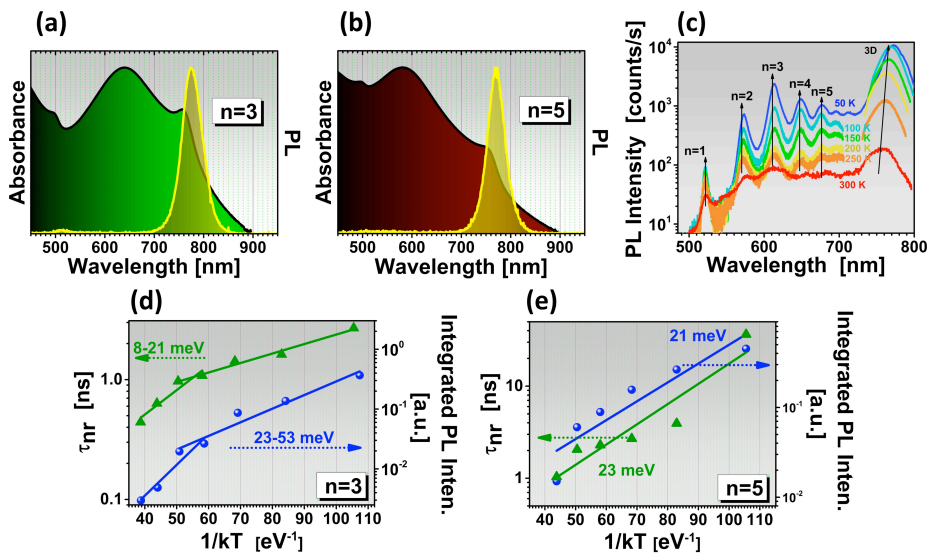

Fig. 2 Optical characterization. (a,b) Steady-state absorbance and PL of 2D/3D perovskite based on $Any_2MA_{n-1}Pb_nI_{3n+1}$ (n=3, 5). PL spectra were acquired under continuous wave excitation at 405 nm. (c) PL spectra registered at different temperatures (under pulsed excitation at 405 nm) in the film prepared nominally for n=2. Contribution of quantum wells (QWs) from n=1 to n=7 (the five most important are labeled) and 3D-like are observed. The arrows indicate that QW-like PL components are not changing significantly (only intensity) with temperature until 250 K as compared to the case of the 3D-like PL band that shifts to the blue. (d,e) stand for the Arrhenius plot of the integrated PL intensity and non-radiative time (radiative and non-radiative times were calculated by assuming unit quantum yield at around 110 K where PL quenching begins and decay time extracted from fitting of the TRPL curves) as a function of 1/kT. The continuous lines correspond to the exponential fit of these experimental data where the slopes stand for the activation energy of the PL quenching.

Temperature dependent PL for a film with nominal value of n=2 exhibits emission peaks that can be assigned as excitonic transitions for layers from n=1-7 (being the most intense that related to n=3) other than the n=infinite band at 760 nm at room temperature, demonstrating the 2D/3D nature of this sample, Fig. 2c. The PL intensity quenching with temperature can be accounted for by an activation energy in the range of 23-53 and 21 meV for n=3 and n=5 samples, respectively (Fig. 2d, e). The temperature dependence of the non-radiative recombination time is also consistent with the PL intensity quenching. TR-PL experiments as function of the temperature shows an exponential dependence where the decay time can be deduced (see Fig. S3). In this way, non-radiative decay time can be extracted from measured decay times and the PL intensity at the different temperature by assuming unit quantum yield at around 110 K, and it is characterized with 8-21 and 23 meV for n=3 and 5 samples, respectively (Fig. 2d,e). These activation energies responsible of the non-radiative recombination mechanism in our samples could be ascribed to the exciton dissociation process as referred for PVK in literature.(25, 26)

In order to obtain information about the dynamics of excited charge carriers and thus the influence of π-free electrons in the anilinium on charge carrier recombination and transfer properties of our samples, we carried out femtosecond (fs) time-resolved transient-absorption (TA) studies of the films. The TA UV-Vis spectra of $Any_2MA_{n-1}Pb_nI_{3n+1}$ (n=3, 5 and 3D) films observed at 0.5 ps pump-probe delay are presented in Fig. 3a. TA spectra of n=3 and 5 show weak excitonic signature in the region of 505 nm, that can be associated to n=1 related excitonic states Fig. 2c. When pump-probe delay time is increased to 2 ps, strong positive (PIA3, 735 nm) and negative (PB2, 770 nm) bands are detected for both n=3 and 5 samples. The positive bands can be related to signal from absorption on free charge carriers, [(27, 28)] while the NIR negative band has been recently observed in the TA spectra of 2D/3D perovskite samples of n≥3, and it was related to photobleaching of low energy states (states related to layers of high n). (26, 29, 30) The comparison of optical properties of 2D/3D and 3D PVK exhibit significant differences. 3D PVK spectrum at 0.5 ps pump-probe delay consist of two bleaching bands at 480 nm (PB1) and 760 nm (PB2), and less intense broad photoinduced absorption (PIA) band (600–750 nm) which are absent in the spectra of our material, indicating that our materials are composed by 2D/3D PVK. The different IR TA behaviour of 2D/3D versus 3D perovskites can be

interpreted on the basis of different charge carrier generation and transfer mechanisms.
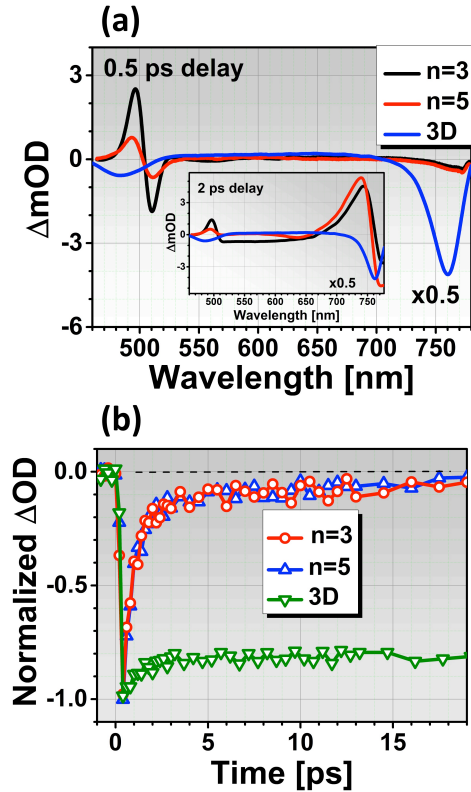

Fig. 3 UV-Vis transient absorption spectra of 2D/3D PVK (n=3, 5 and 3D) films at 0.5 ps pump-probe delay. The inset shows the transient spectra at 2 ps pump-probe delay. For clarity, the intensity of the spectrum of 3D perovskite film (3D) is multiplied by factor 0.5. (c) Transient absorption decays of 2D/3D perovskite upon excitation at 400 nm and observation at 485 nm (3D film) and 510 nm (n=3 and 5). The TA signals were obtained upon excitation at 400 nm using a fluence of the absorbed photons of 8.2×10^{12} ph/cm^2 (3D film) and 9.0×10^{12} ph/cm^2 (2D/3D films). The solid lines in (c) are from the best biexponential fits. The explored films were fabricated at 130 °C.

While in 3D MAPbI$_3$ perovskite, the charges are free after excitation and relax within <1 ps, in 2D/3D perovskite the charges are primary generated in the excitonic form due to the intrinsically higher exciton binding energy.(31, 32) For samples with n≥3, it is expected that these excitons dissociate and are transferred to energetically lower states,(26, 29) that is in agreement with the presented temperature-dependent measurements, Fig. 2d, e. The Fig. 3b shows the normalized representative fs-transients for n=3 and 5 at 510 nm, and 3D perovskite at 485 nm. These decays were well fitted using a bi-exponential function (Table S1), which has been successfully applied to analogous systems.

(26, 29, 30, 33) The dynamics of all the samples show fast initial decay followed by a slower decrease of the residual signal intensity. For the transients of all 2D/3D samples, we got similar time constants of ~ 0.5 and 18 ps, although their components differ in amplitudes, indicating different influence of the most probably faster/slower exciton deactivation mechanism among the samples.(26) The n=3 and 5 samples show no offset and high amplitude of the faster decay component (87% and 89%, respectively), thus almost 90% of the TA signal are lost within 1 ps. Thus, excitons are extremely effectively deactivated within these samples. Additionally, the TA dynamics gated at 735 and 770 nm exhibit rising time constants of ~ 0.5 and 40 ps and very slow decays (taken here only as offset). The values of rising amplitudes are comparable to the ones detected at 500 nm region for both samples (A1=88% and A2=12%, respectively, see Table S2, Fig.s S4 a,b). The difference between the second time constants observed in both spectral regions (18 *Vs* 40 ps) can be interpreted in terms of the presence of trapping/releasing or other processes that could extend transport time of the charges originating from the more stable excitons. However, deeper studies beyond this work are needed. The similarity between the excitons decay at 500 nm region and rise of the TA NIR signal are a strong support to the expected mechanism of exciton deactivation in our samples based on excitons dissociation, followed by a transfer of the free charges to lower energy states.(26)

For further clarification of the charge carrier processes in our samples, the TA measurements of 2D/3D PVK n=5 sample upon excitation at 500, 600 and 700 nm were done and compared to the one obtained using 400 nm excitation (Fig. S4c-e). The TA spectra at 2 ps pump-probe delay show comparable spectral shapes (minimal signal in visible spectra interval and strong signal in red and IR), suggesting that independently on excess energy the photoexcited charges are transferred to states at 770 nm (Fig. S2c). These results suggest that the excited charges are transferred to common low energy states, as we observe previously.(19) The TA dynamics observed at 770 nm using all excitations are presented in Fig. S4d and S4e, respectively. As can be seen, the initial rise dynamics, that are related to charge transport from higher energy states, are similar for excitations upon 400 and 500 nm (τ = 0.5 ps) and getting shorter for further increase of excitation wavelength (τ is 0.3 ps and 0.2 ps for 600 and 700 nm, respectively). Moreover, only TA dynamics obtained using 400 and 500 nm pump wavelength show secondary rise component (~ tens of ps). The subsequent slow decay does not depend

much on the excitation wavelength. This behavior shows that only layers in $Any_2MA_{n-1}Pb_nI_{3n+1}$ (n=1) are able create stable excitons in our samples, while only excitation at 400 and 500 nm can create excitons in these layers. Excitation of thicker layers results in fast dissociation of initial excitons and their transfer to energetically lower states. A decrease of excitation wavelength from 600 to 700 nm is shortening the rising time constants due to closer position of excited and final state of the transfer. The absence of signals at 505 nm using 600 and 700 nm excitation is also proving differences between low energy states in 2D/3D and bulk 3D PVK, since the signal at 480 nm (PB1) in 3D PVK, can be generated by 600 nm excitation.[34]

Summarizing, the ultrafast dynamics of exited 2D/3D samples of $Any_2MA_{n-1}Pb_nI_{3n+1}$ suggests large excitons deactivation in the samples of n≥3. This statement is supported by (i) the absence of exciton states related to n>1, (ii) very low concentration of excitons after 1 ps for the samples having n≥3 (spectral region ~500 nm), and (iii) strong TA signal from PIA and negative band in NIR region. The similar TA decays dynamics of both multi-layered samples and especially comparable values of TA signals at 735 nm, suggest that the excitons in the sample of n=3 are able to dissociate with an efficiency similar to that of n=5. This direct comparison is possible because the samples are excited using the same fluence of the absorbed photons. In addition, the amplitude (~12%) of the second TA rise is lower and faster than the reported for non-conjugated 2D/3D perovskite samples (~ few tens of percentage and from tens to hundreds of ps). (26, 29, 30, 33) This difference can be also interpreted in terms of a higher efficiency of excitons dissociation and charge transfer from initial excitonic states to the low energy ones, related to thicker perovskite layers (high n) in $Any_2MA_{n-1}Pb_nI_{3n+1}$ sample, in contrast to other 2D/3D perovskite films.

In the next step we focus on the characterization and fabrication of $AnyPb_5$ 2D/3D PVK based solar cell devices through modified hot-casting method.(11, 19) The choice of n=5 as sensitizer was made not only on the basis that the photovoltaic performance of solar cells based on 2D/3D perovskites increases with n(18) but also considering that the long term stability of the devices decreases with n, as a consequence of the decrease of concentration of hydrophobic cations. Considering the deficient coating by our

2D/3D PVK material previously discussed, and with the aim of improves it, we fabricated thin films through a scanning of temperatures from 110 to 190 °C.(35)

The structural properties of the 2D/3D perovskite layers formed at different substrate temperatures have been analyzed by XRD. The XRD patterns are shown in Fig. S5a. The obtained values matches perfectly with those described in past section for n=5. In addition, the reflection peak observed at 6.9° confirms the 2D/3D nature of this material. (17) However, a greater crystallinity´s degree of the material is observed when the pre-heating temperature of the substrates increases, which is supported by the Full Width-Half Maximum (FWHM) trends. The FWHM of the (111) reflection, at 14.2°, reduces from 0.232°, for perovskite films processed at 100 °C, to 0.099° for films treated at 170 °C, Fig. S5b. However, when the temperature reaches 170 °C and above, it is possible to see diffraction peaks at 12.72°, which can be associated to PbI_2 traces.

The morphology and electrical characteristics of the $AnyPb_5$ films (T=110, 150 and 190 °C) has been investigated by measuring the topography and also the local current via an atomic force microscopy (AFM). Fig. 4a, c and e show the topographical AFM maps of the samples processed at 110, 150 and 190 °C, covering the whole temperature range chosen in this work.
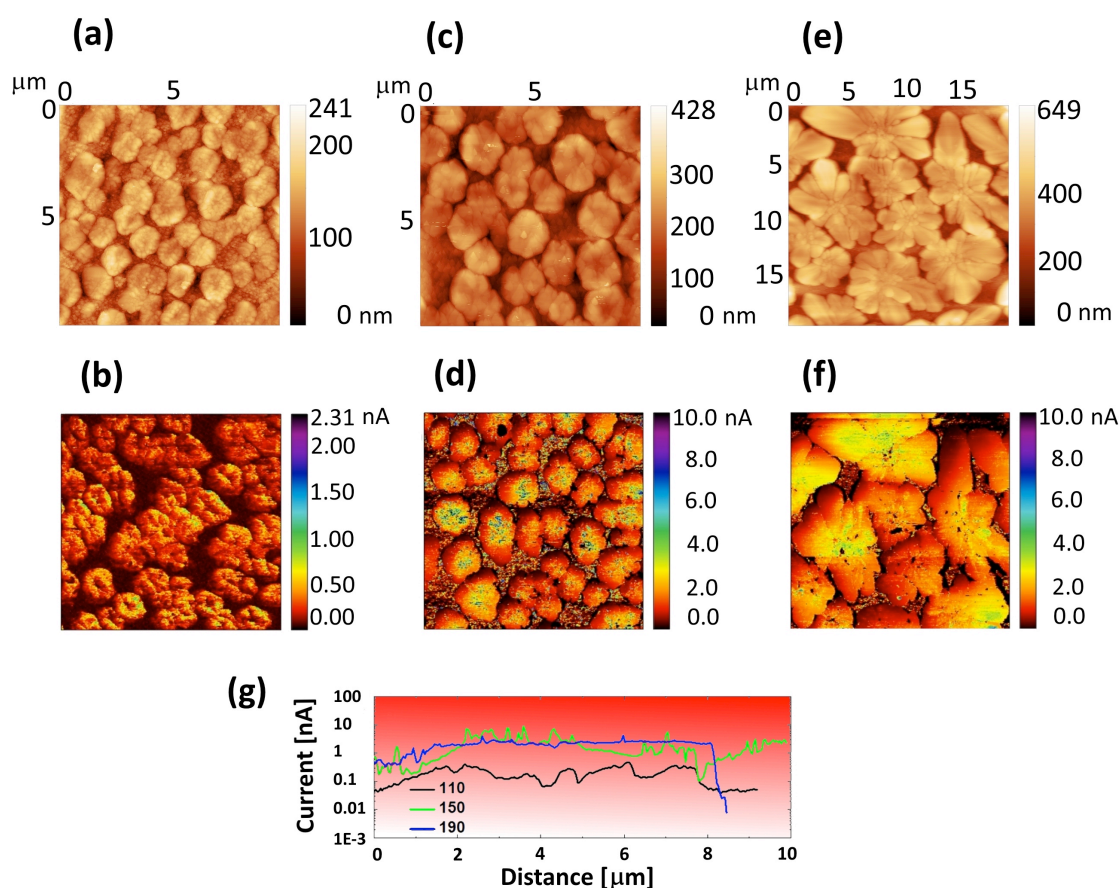
Fig. 4 Atomic force microscopy (AFM) and conducting AFM (c-AFM) maps of 2D/3D perovskites AnyPb$_5$ synthesized at different processing temperature 110 °C (a and b), 150 °C (c and d), and 190 °C (e and f). The AFM images show a scale of 20 × 20 mm. The c-AFM images are taken at an applied bias of 4V, showing absolute values of local current. (g) Local current measured at the three different perovskite samples.

The both AFM and SEM images suggest that the vertical growth of the perovskite grains occurs through of nucleation points along the surface of mesoporous TiO$_2$, which unfortunately is not completely covered. The 2D/3D perovskite grown on top of mesoporous TiO$_2$ presents a leaf-like shape, with its size increasing as temperature rise, explaining the higher crystallinity observed by the reduction of XRD FWHM. The determined grain size ranging from 1.51±0.04, 2.26±0.10 and 7.1±0.4 μm for films prepared at 110, 150 and 190 °C, respectively (Fig. S6). At higher temperature the surface coverage improves due to the larger grain size, also influencing the surface roughness. The calculated root mean square (rms) roughness over a number of grains is 11.2±1.0, 13.6±3.3, and 17.4±3.0 nm for 110, 150, and 190 °C, respectively; while the

coating´s percentage of the surface it was determined to be ≈57% for the films prepared at 110 °C, ≈67% for the prepared at 150 °C and ≈79% for those prepared at 190 °C (Fig. S7).

Considering that in 2D/3D perovskites the transport properties are severely reduced, in comparison with 3D counterparts, owing to the presence of bulky organic cation, we have measured local current maps via a conducting AFM under N_2 flow at an applied bias 4 V (Fig. 4b, d and f). Interestingly, we note nearly an order of magnitude increase in local current for perovskite films treated at higher temperature, see Fig. 4g. Systematically, in all the samples, we note a lower current at grain boundaries (dark regions), suggesting that grain boundaries limit the performance and increase the trap density in the films. We also note a minor variation of local current within a single leaf structure (Fig. S8), suggesting a highly polycrystalline surface, probably due to mixed phases with different n and/or crystalline orientations. This is further confirmed from the surface potential maps, recorded via Kelvin Probe Force Microscopy (KPFM) (Fig. S8), demonstrating a small variation of the surface potential up to 300 mV for an individual grain. We noted a jump in the surface potential value at the grain boundary which changes up to 1 V on the film region with no perovskite (or on the TiO_2 surface).

Absorbance measurements were carried out to determine potential variations in optical properties as consequence of the different temperatures of fabrication. The Fig. 5 displays the absorbance spectra of the fabricated $AnyPb_5$ films. All of them showed identical spectral features with continuous absorption rise in IR with decreasing wavelength (maximum at 750 nm) and shoulder at around 505 nm. The appearance of that excitonic peak can be due to trace amounts of n=1 phase, which is possible to detect as a consequence of the great stability that the exciton exhibit even at room temperature.(8) The position of the absorption maximum in IR is in agreement with TAS measurements (negative bleach Fig. 3b) and is probably related to the presence of LES states. (23) In addition to that, the pronounced Urbach tail observed at 800-900 nm can be related to other low energy localized states caused by the structural in-homogeneities of the samples. Interestingly, even though spectral profile have identical features, it is possible to see a systematic increase in the absorption properties as the fabrication´s temperature rise. Additionally, the Fig. 5 show as the films becomes darker

as the temperature upsurge. Considering that spectral profile of all the samples display the same optical properties, the increase in the absorption can be related to both better surface coverage and a thicker film, as can be observed previously by AFM/SEM microscopies.
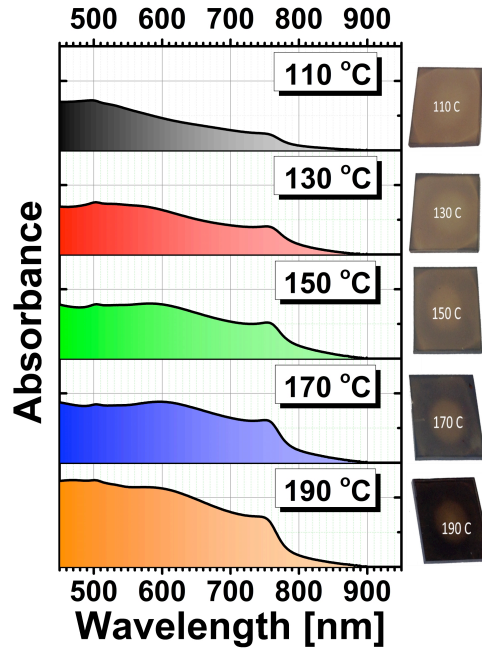

Fig. 5 Absorbance spectra of 2D/3D perovskites AnyPb$_5$ films prepared at different temperatures.

After fundamental characterization of the perovskite material, the photovoltaic performance of PSC fabricated with different temperatures of substrate pre-heating has been analyzed.(11, 35) The fabrication of our 2nd generation of devices was carried out, with n-i-p architecture was carried out i.e., FTO, compact and mesoporous layers TiO$_2$, 2D/3D perovskite with n=5, spiro-OMeTAD as hole selecting contact and gold. Fig. 6 shows the current-potential (J-V) curves and the photovoltaic parameters, for champion devices, for each of the temperatures evaluated. Regarding the evaluation of manufacturing temperature, J-V curves for champion devices show a systematic increase in the PCE with increasing temperature from 110 to 190 °C. The PCE values obtained are 5.96% for device prepared at 110 °C and 7.63% for the device fabricated at 190 °C. The principal factor that contributes to the improvement of PCE while increasing the crystallization temperature is the photocurrent J$_{sc}$, up from 10.39 mAcm^{-2} for T=110 °C to 13.79 mAcm^{-2} for T=190 °C. Higher values of photocurrent have been

reported for 2D/3D perovskites with relatively low n, (11, 36) however the value reported here is one of the highest obtained for low-n layered perovskites. For comparison, when was used butylammonium iodide (BAI, pure phase, n=5) instead anilinium, the maximum value obtained for J_{sc} was 11.67 mAcm^{-2}. Respect another features that characterize the photovoltaic performance, fill factor shows values ~70%, which tends to decrease as the temperature increases; while the V_{oc} remains between 805 and 822 mV. The low V_{oc} observed in our results with respect to previously reported values for 3D is probably due to a higher recombination rate as it has been studied by impedance spectroscopy, (37-39) see Fig. S9, however, a complete study will be reported separately.
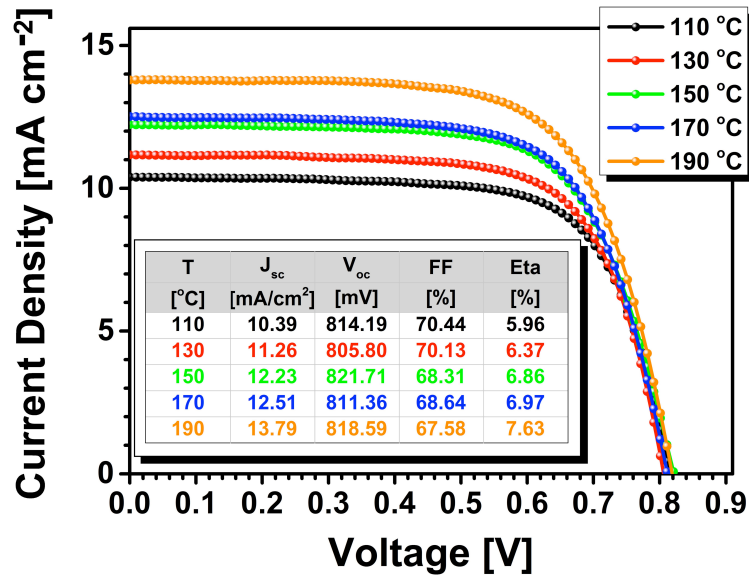

T	J_{sc}	V_{oc}	FF	Eta
[°C]	[mA/cm^2]	[mV]	[%]	[%]
110	10.39	814.19	70.44	5.96
130	11.26	805.80	70.13	6.37
150	12.23	821.71	68.31	6.86
170	12.51	811.36	68.64	6.97
190	13.79	818.59	67.58	7.63

Fig. 6 J-V curves for champion devices of 2D/3D perovskites AnyPb$_5$ at each evaluated temperature. The table shows the photovoltaic values for champion devices.

Briefly, 2D/3D samples present lower recombination resistance (higher recombination rate) than standard 3D perovskite at high applied bias, where recombination current is important, see Fig. S9a. Different recombination pathways are possible. Among them, the incomplete surface coverage of TiO$_2$ mesoporous layer by the perovskite film is affecting deleteriously cell performance.(40) This point indicates that there is more room for improvement of anilinium based 2D/3D perovskites by the control of crystal nucleation/growth processes. It is also interesting to point out that low frequency

capacitance, associated with charge accumulation driven by ionic diffusion, (38, 41) is significantly lower than in 3D samples, see Fig. S9b, pointing to a lower ion diffusion in 2D/3D materials.

Interestingly average values obtained for devices fabricated at different temperatures do not follow the same trend than champion cells; see Table S3 and Fig. S10. Concerning the average PCE values, an improvement is evident with increase in the temperature; however, when the processing temperature increases to 170 °C and above, the dispersion of the obtained results increases causing that the average PCE gradually decreases. This variability observed in the results we suggest is directly related to the experimental conditions. Pre-heated substrates are quickly transferred from the hot plate to the spin coater, immediately the perovskite precursor solution is added and the spin coating process start. When the samples are in a low temperature range, e.g., 110 to 150 °C, the change of temperatures is less abrupt and the results can be more reproducible compared to the higher temperature range.

Even though the introduction of bulky cation with high value of ε suggest a stronger interaction with water than cations with low value of ε (and therefore lees moisture stability), we carried out a stability test under ambient conditions for the fabricated devices. Their stability was compared with a pure 3D PVK based solar cells, (Fig. S11). The devices were kept under ambient humidity over 40% for a period of 288 h. Interestingly, the devices prepared between 110 and 150 °C, exhibit higher long term stability than 3D perovskite based devices stored at similar conditions. In the other hand, the results showed that the devices fabricated with the highest temperatures (170 and 190 °C) exhibit lower long term stability than 3D perovskites. Very recently, we have shown that the presence of a reduced amount of moisture during the perovskite deposition processes is positive from the stability point of view.(42) In this way, the high temperature utilized in the high temperature regime could avoid the presence of this little humidity, preventing its beneficial role.

In conclusion, we demonstrate that the use of a conjugated anilinium cation, with a cloud of free and polarizable π-electrons, in the preparation of 2D/3D PVK led to obtain a material with optical and electrical properties improved. The determinant factor was the tuning of dielectric contrast between inorganic and organic layers, which has direct influence in the decrease of exciton binding energy. Through steady state and time-

resolved absorption experiments we have proved high efficiency of initially generated exciton dissociation even for samples with low n (about 3) and thus high potential of these structures in photovoltaics. The scanning of temperature´s fabrication stated a relation between temperature and size/crystallinity of the material. Thus it was observed a gradual increment in the size of crystallites on going from low to high fabrication´s temperatures. When the crystallinity of the material was improved through the temperature and a better coverage of the film was achieved, the PCE it got better. Importantly, the higher J_{sc} observed, comparing to the reported values, is a strong indicative of both: 1) a lower exciton binding energy by tuning of dielectric contrast between wells and barriers and 2) an increase in the electronic transport properties of this material. Surprisingly, in spite of the intrinsic nature of the employed cation suggest an important interaction with water, the devices fabricated with 2D/3D perovskite showed a higher stability (near to 70%) after 288 h than 3D perovskite (less than 40%) under the same period and environmental conditions. Further improvement on the performance of anilinium based 2D/3D perovskites can be anticipated if higher control of the nucleation and crystal growth conditions are obtained, work that it is currently in progress.

Conflict of interest
There are no conflicts to declare.

ESI available
Chemical representation of structure of cations used in the fabrication of 2D materials, SEM images of surface coatings for n=3 and 5 as well as n=5 (at several temperatures). Details of PL, TRPL and TAS for n=3 and 5 and 3D films. XRD patterns and FWHM

determination for n=5 at several temperatures. AFM details. Impedance spectroscopy. Statistical distribution of photovoltaic parameters at different temperatures of fabrication. Stability response to environmental conditions

References

1. Adinolfi V, Peng W, Walters G, Bakr OM, Sargent EH. The Electrical and Optical Properties of Organometal Halide Perovskites Relevant to Optoelectronic Performance. Adv Mater. 2018 Jan;30(1). PubMed PMID: 29024039.
2. Seok SI, Grätzel M, Park N-G. Methodologies toward Highly Efficient Perovskite Solar Cells. Small. 2018:1704177-n/a.
3. Yang WS, Park B-W, Jung EH, Jeon NJ, Kim YC, Lee DU, et al. Iodide management in formamidinium-lead-halide–based perovskite layers for efficient solar cells. Science. 2017;356(6345):1376-9.
4. Bella F, Griffini G, Correa-Baena JP, Saracco G, Gratzel M, Hagfeldt A, et al. Improving efficiency and stability of perovskite solar cells with photocurable fluoropolymers. Science. 2016 Oct 14;354(6309):203-6. PubMed PMID: 27708051.
5. Bi D, Gao P, Scopelliti R, Oveisi E, Luo J, Gratzel M, et al. High-Performance Perovskite Solar Cells with Enhanced Environmental Stability Based on Amphiphile-Modified $CH_3 NH_3 PbI_3$. Adv Mater. 2016 Apr 20;28(15):2910-5. PubMed PMID: 26880116.
6. Mitzi DB. Synthesis, Structure, and Properties of Organic-Inorganic Perovskites and Related Materials. NJ, USA: John Wiley & Sons; 1999.
7. Hong X, Ishihara T, Nurmikko AV. Dielectric confinement effect on excitons in ${\mathrm{PbI}}_{4}$-based layered semiconductors. Physical Review B. 1992 03/15/;45(12):6961-4.
8. Ishihara T, Takahashi J, Goto T. Exciton state in two-dimensional perovskite semiconductor (C10H21NH3)2PbI4. Solid State Communications. 1989 1989/03/01/;69(9):933-6.
9. Smith IC, Hoke ET, Solis-Ibarra D, McGehee MD, Karunadasa HI. A Layered Hybrid Perovskite Solar-Cell Absorber with Enhanced Moisture Stability. Angewandte Chemie International Edition. 2014;53(42):11232-5.
10. Stoumpos CC, Cao DH, Clark DJ, Young J, Rondinelli JM, Jang JI, et al. Ruddlesden–Popper Hybrid Lead Iodide Perovskite 2D Homologous Semiconductors. Chemistry of Materials. 2016 2016/04/26;28(8):2852-67.
11. Tsai H, Nie W, Blancon J-C, Stoumpos CC, Asadpour R, Harutyunyan B, et al. High-efficiency two-dimensional Ruddlesden–Popper perovskite solar cells. Nature. 2016 07/06/online;536:312.
12. Cao DH, Stoumpos CC, Farha OK, Hupp JT, Kanatzidis MG. 2D Homologous Perovskites as Light-Absorbing Materials for Solar Cell Applications. Journal of the American Chemical Society. 2015 Jun 24;137(24):7843-50. PubMed PMID: 26020457.
13. Stoumpos CC, Soe CMM, Tsai H, Nie W, Blancon J-C, Cao DH, et al. High Members of the 2D Ruddlesden-Popper Halide Perovskites: Synthesis, Optical Properties, and Solar Cells of $(CH_3(CH_2)_3NH_3)_2(CH_3NH_3)_4Pb_5I_{16}$. Chem. 2017;2(3):427-40.
14. Cheng P, Xu Z, Li J, Liu Y, Fan Y, Yu L, et al. Highly Efficient Ruddlesden–Popper Halide Perovskite PA2MA4Pb5I16 Solar Cells. ACS Energy Letters. 2018 2018/08/10;3(8):1975-82.
15. Grancini G, Roldan-Carmona C, Zimmermann I, Mosconi E, Lee X, Martineau D, et al. One-Year stable perovskite solar cells by 2D/3D interface engineering. Nature communications. 2017 Jun 1;8:15684. PubMed PMID: 28569749. Pubmed Central PMCID: 5461484.

16.   Koh TM, Shanmugam V, Schlipf J, Oesinghaus L, Müller-Buschbaum P, Ramakrishnan N, et al. Nanostructuring Mixed-Dimensional Perovskites: A Route Toward Tunable, Efficient Photovoltaics. Advanced Materials. 2016;28(19):3653-61.

17.   Cohen B-E, Wierzbowska M, Etgar L. High Efficiency and High Open Circuit Voltage in Quasi 2D Perovskite Based Solar Cells. Advanced Functional Materials. 2017;27(5):1604733-n/a.

18.   Quan LN, Yuan M, Comin R, Voznyy O, Beauregard EM, Hoogland S, et al. Ligand-Stabilized Reduced-Dimensionality Perovskites. Journal of the American Chemical Society. 2016 Mar 2;138(8):2649-55. PubMed PMID: 26841130.

19.   Rodríguez-Romero J, Hames BC, Mora-Seró I, Barea EM. Conjugated Organic Cations to Improve the Optoelectronic Properties of 2D/3D Perovskites. ACS Energy Letters. 2017 2017/09/08;2(9):1969-70.

20.   Smith MD, Pedesseau L, Kepenekian M, Smith IC, Katan C, Even J, et al. Decreasing the electronic confinement in layered perovskites through intercalation. Chemical science. 2017 Mar 1;8(3):1960-8. PubMed PMID: 28451311. Pubmed Central PMCID: 5384564.

21.   Soe CMM, Nie W, Stoumpos CC, Tsai H, Blancon J-C, Liu F, et al. Understanding Film Formation Morphology and Orientation in High Member 2D Ruddlesden–Popper Perovskites for High-Efficiency Solar Cells. Advanced Energy Materials. 2018;8(1):1700979-n/a.

22.   Lian J, Wang Q, Yuan Y, Shao Y, Huang J. Organic solvent vapor sensitive methylammonium lead trihalide film formation for efficient hybrid perovskite solar cells. Journal of Materials Chemistry A. 2015;3(17):9146-51.

23.   Blancon JC, Tsai H, Nie W, Stoumpos CC, Pedesseau L, Katan C, et al. Extremely efficient internal exciton dissociation through edge states in layered 2D perovskites. Science. 2017 Mar 24;355(6331):1288-92. PubMed PMID: 28280250.

24.   Gauthron K, Lauret JS, Doyennette L, Lanty G, Al Choueiry A, Zhang SJ, et al. Optical spectroscopy of two-dimensional layered (C6H5C2H4-NH3)2-PbI4 perovskite. Opt Express. 2010 2010/03/15;18(6):5912-9.

25.   Wu K, Bera A, Ma C, Du Y, Yang Y, Li L, et al. Temperature-dependent excitonic photoluminescence of hybrid organometal halide perovskite films. Physical Chemistry Chemical Physics. 2014;16(41):22476-81.

26.   Shang Q, Wang Y, Zhong Y, Mi Y, Qin L, Zhao Y, et al. Unveiling Structurally Engineered Carrier Dynamics in Hybrid Quasi-Two-Dimensional Perovskite Thin Films toward Controllable Emission. The Journal of Physical Chemistry Letters. 2017 2017/09/21;8(18):4431-8.

27.   Piatkowski P, Cohen B, Javier Ramos F, Di Nunzio M, Nazeeruddin MK, Grätzel M, et al. Direct monitoring of ultrafast electron and hole dynamics in perovskite solar cells. Physical Chemistry Chemical Physics. 2015;17(22):14674-84.

28.   Xing G, Mathews N, Sun S, Lim SS, Lam YM, Grätzel M, et al. Long-Range Balanced Electron- and Hole-Transport Lengths in Organic-Inorganic $CH_3NH_3PbI_3$. Science. 2013;342(6156):344-7.

29.   Liu J, Leng J, Wu K, Zhang J, Jin S. Observation of Internal Photoinduced Electron and Hole Separation in Hybrid Two-Dimentional Perovskite Films. Journal of the American Chemical Society. 2017 2017/02/01;139(4):1432-5.

30.   Xing G, Wu B, Wu X, Li M, Du B, Wei Q, et al. Transcending the slow bimolecular recombination in lead-halide perovskites for electroluminescence. Nature communications. 2017 02/27/online;8:14558.

31.   Gélvez-Rueda MC, Hutter EM, Cao DH, Renaud N, Stoumpos CC, Hupp JT, et al. Interconversion between Free Charges and Bound Excitons in 2D Hybrid Lead Halide Perovskites. The Journal of Physical Chemistry C. 2017 2017/11/30;121(47):26566-74.

32.   Straus DB, Kagan CR. Electrons, Excitons, and Phonons in Two-Dimensional Hybrid Perovskites: Connecting Structural, Optical, and Electronic Properties. The Journal of Physical Chemistry Letters. 2018 2018/03/15;9(6):1434-47.

33.   Wang N, Cheng L, Ge R, Zhang S, Miao Y, Zou W, et al. Perovskite light-emitting diodes based on solution-processed self-organized multiple quantum wells. Nature Photonics. 2016 09/26/online;10:699.

34.   Galar P, Piatkowski P, Ngo TT, Gutiérrez M, Mora-Seró I, Douhal A. Perovskite-quantum dots interface: Deciphering its ultrafast charge carrier dynamics. Nano Energy. 2018 2018/07/01/;49:471-80.

35.   Nie W, Tsai H, Asadpour R, Blancon J-C, Neukirch AJ, Gupta G, et al. High-efficiency solution-processed perovskite solar cells with millimeter-scale grains. Science. 2015;347(6221):522-5.

36.   Zhang X, Wu G, Fu W, Qin M, Yang W, Yan J, et al. Orientation Regulation of Phenylethylammonium Cation Based 2D Perovskite Solar Cell with Efficiency Higher Than 11%. Advanced Energy Materials. 2018:1702498-n/a.

37.   Guerrero A, Garcia-Belmonte G, Mora-Sero I, Bisquert J, Kang YS, Jacobsson TJ, et al. Properties of Contact and Bulk Impedances in Hybrid Lead Halide Perovskite Solar Cells Including Inductive Loop Elements. The Journal of Physical Chemistry C. 2016 2016/04/21;120(15):8023-32.

38.   Zarazua I, Han G, Boix PP, Mhaisalkar S, Fabregat-Santiago F, Mora-Seró I, et al. Surface Recombination and Collection Efficiency in Perovskite Solar Cells from Impedance Analysis. The Journal of Physical Chemistry Letters. 2016 2016/12/15;7(24):5105-13.

39.   Zarazúa I, Sidhik S, Lopéz-Luke T, Esparza D, De la Rosa E, Reyes-Gomez J, et al. Operating Mechanisms of Mesoscopic Perovskite Solar Cells through Impedance Spectroscopy and J–V Modeling. The Journal of Physical Chemistry Letters. 2017 2017/12/21;8(24):6073-9.

40.   Fakharuddin A, Schmidt-Mende L, Garcia-Belmonte G, Jose R, Mora-Sero I. Interfaces in Perovskite Solar Cells. Advanced Energy Materials. 2017;7(22):1700623.

41.   Zarazua I, Bisquert J, Garcia-Belmonte G. Light-Induced Space-Charge Accumulation Zone as Photovoltaic Mechanism in Perovskite Solar Cells. The Journal of Physical Chemistry Letters. 2016 2016/02/04;7(3):525-8.

42.   Contreras-Bernal L, Aranda C, Valles-Pelarda M, Ngo TT, Ramos-Terrón S, Gallardo JJ, et al. Homeopathic Perovskite Solar Cells: Effect of Humidity during Fabrication on the Performance and Stability of the Device. J Chem Phys C. 2018 2018/03/15;122(10):5341-8.